Sustainable Energy & Fuels

Out-of-Plane Transient Thermal Conductivity Measurements for Bulk Semiconducting Conjugated Polymers using Fast Scanning Calorimetry

Journal:	*Sustainable Energy & Fuels*
Manuscript ID	SE-ART-10-2022-001413.R1
Article Type:	Paper
Date Submitted by the Author:	23-Nov-2022

Complete List of Authors:	Zhao, Haoyu; University of Southern Mississippi, School of Polymer Science and Engineering Prine, Nathaniel; University of Southern Mississippi, School of Polymer Science and Engineering Ma, Guorong; University of Southern Mississippi, School of Polymer Science and Engineering Zhang, Yongcao; King Abdullah University of Science and Technology Haque, Md Azimul; King Abdullah University of Science and Technology Baran, Derya; King Abdullah University of Science and Technology Gu, Xiaodan; University of Southern Mississippi, School of Polymer Science and Engineering

ARTICLE

Out-of-Plane Transient Thermal Conductivity Measurements for Bulk Semiconducting Conjugated Polymers using Fast Scanning Calorimetry

Received 00th January 20xx,
Accepted 00th January 20xx

DOI: 10.1039/x0xx00000x

Haoyu Zhao[a], Nathaniel Prine[a], Guorong Ma[a], Yongcao Zhang[b], Md Azimul Haque[b], Derya Baran[b] and Xiaodan Gu[a]*

Thermal conductivity directly impacts the performance of organic thermoelectric devices which convert heat into useful electricity. However, quantitatively measuring the bulk thermal conductivity of conjugated polymers remains complicated and hinders the rational design of advanced organic thermoelectric materials and true key performance calculation, Figure of Merit (ZT). The novel fast scanning calorimetry is adopted to address these limitations for the first time by measuring the heat conduction for conjugated polymeric films. Out of the plane thermal conductivity of polydiketopyrrolopyrrole (PDPPT) based polymers and poly (3-hexylthiophene) (P3HT) films are quantitatively captured by directly monitoring heat transfer through tens of micrometer thick polymer films. For undoped polymers, PDPPT displayed a higher out of plane thermal conductivity than P3HT (0.263 vs. 0.168 W/mK) due to higher backbone rigidity. After doping with 2,3,5,6-tetrafluoro-7,7,8,8-tetracyanoquinodimethane (F4TCNQ), the thermal conductivity of doped PDPPT first increases at lower doping levels up to 5 wt%, then decreases at higher doping levels, which can be attributed to changes in the degree of crystallinity for doped films quantified by X-ray scattering measurements. The highest thermal conductivities are found for doping levels ranging from of 2.5 % for P3HT (0.276 W/mK) and 5 % PDPPT (0.420 W/mK) primarily due to enhanced degree of crystallinity. This work further facilitates the rational design of future organic thermoelectric materials by optimizing the thermal conductivity using controlled doping.

1. Introduction

The urgent need for renewable energy sources and growing concerns over climate change contributes to the growing interest in thermoelectric materials capable of converting excess or waste heat into useful electrical energy.[1–4] The conversion efficiency of heat into electricity is quantified by the dimensionless term (*ZT)*, which is described by the following equation:

$$ZT \sim \frac{S^2 \sigma T}{K} \qquad (1)$$

where S is the Seebeck coefficient, σ is the electrical conductivity, T is the absolute temperature, and K is the thermal conductivity. Thus, one can improve the device efficiency either with a higher power factor ($S^2*\sigma$) term[5] or a lower thermal conductivity term.[6,7]

Thermoelectric material properties can be commonly controlled using dopants to enhance device performance.[8,9] While the dopants can be added to conjugated polymers (CPs), the dopant efficiency[10] is limited by the miscibility of the dopants and CPs. Consequently, excess doping results in unreacted dopants and restricts thermal conductivity. The miscibility between dopants and CPs can be increased by incorporating polar side chains on the polymer backbone to encourage polymer-dopant interactions.[11] This results in higher doping efficiency and enhanced electrical conductivity for thermoelectric materials. Additionally, other synthetic post-polymerization modifications have been reported to improve thermoelectric device performance. These methods include 1) the backbone structural modification of pyrazine-flanked DPP derivatives with deep lowest unoccupied molecular orbital (LUMO) level,[12] 2) the addition of halogen atoms to the polymer backbone,[13] and 3) side chain engineering by installing short side chains for self-doped CPs[14]. These efforts demonstrate that higher doping levels and enhanced power factors can be achieved.[15–18] While most works related to CPs doping in literature are centered on electrical properties and the Seebeck coefficient characteristics, the role of dopants in thermal conductivity remains controversial, depending on the system and amount of added dopants. Therefore, it remains unknown if the thermal conductivity of CPs could be enhanced[19–22] or reduced[23–25] or even unchanged[26,27] by the introduction of dopant molecules. This controversy remains due to challenges in measuring thermal conductivity in conjugated polymeric thin films.

Current characterization techniques for steady-state thermal conductivity include slab methods and suspended

[a] School of Polymer Science and Engineering, The University of Southern Mississippi, 118 College Drive, Hattiesburg, MS 39406, United States of America
*E-mail: xiaodan.gu@usm.edu
[b] Physical Sciences and Engineering Division, KAUST Solar Center, King Abdullah University of Science and Technology, Thuwal 23955, Saudi Arabia
Electronic Supplementary Information (ESI) available: See DOI: 10.1039/x0xx00000x

resistance thermometer tests. A suspended resistance thermometer tests a specimen that is bridged between two heater/sensor islands to conduct heat caused by steady-state heat flow and is widely adopted for testing thermal conductivity for nanofibers[28,29]. On the contrary, the thermal wave technique[30–32], time-domain thermoreflectance (TDTR)[33–36] and 3-Omega (3ω) method[37], have been widely used to investigate the transient thermal conductivity for thin film. The thermal wave method measures the thermal diffusivity by recording the phase shift of an oscillating temperature wave traveling between two signal receivers. Although both in-plane and out-of-plane[38] thermal diffusivity can be measured, this technique typically requires large specimens (e.g. 10 by 10 mm) and thick films (1 to 1000 μm).[39] Since the thermal wave must travel a long distance to obtain reasonable data, the accuracy of the measurement is perturbed by any small fluctuations in film thickness over a wide area. TDTR is another popular method for measuring thermal conductivity for both conventional polymers [40], and conjugated polymers (P3HT[41–43] and poly(4,8-bis-alkyloxybenzo[1,2-b:4,5-b′]dithiophene-2,6-diyl-alt-(alkylthieno[3,4-b]thiophene-2-carboxylate)-2,6-diyl) (PBDTTT)[44]). The temperature gradient triggered by laser pulses is used to probe the thermal conductivity[33–36,45]. The TDTR method is capable of measuring both in-plane[46] and out-of-plane[47] thermal conductivity for thin films but surface treatment must be applied for samples. For example, both substrate and sample surface require coating of aluminums to amplify signals. In addition, the advantages of this method include characterizations of multiple thermal properties (thermal conductivity, interfacial thermal conductance, heat capacity) by varying time domains,[48] and less complicated sample preparation. The shortcomings of this technique are from the complex experimental setup and data treatment. Moreover, the specimen must have a very smooth surface because microvoids could lower the accuracy of TDTR measurements.[49] The 3ω method is another popular measurement technique to obtain in-plane and out-of-plane thermal conductivity for thin films.[37,50–52] The 3ω method, has a simple experimental setup where a metal heating line is placed on top of a specimen film supported by a substrate.[52] The heating wire is controlled by an alternating current at specific frequencies to provide heat flux to the specimen surface. The experimental geometry of 3ω method significantly reduced the errors associated with radiation and convective heat loss.[48] However, complicated sample preparation is required, especially for conjugated materials, where additional insulating layers are applied on the samples surface so that the sample is electrically isolated from the metallic heater. The insulating layers will cause thermal resistance and eventually influence the measurement sensitivity and accuracy.[53] Another concerns for TDTR and 3ω techniques are the usage of metallic transducer layers or metallic heater/sensor microfabrication, where the surrounding materials may significantly impact the thermal properties of testing samples.[54,55]

Herein, we demonstrated the first calorimetric based technique[56,57] using differential scanning chip calorimetry (Flash-DSC) to directly probe the out-of-plane thermal conductivity of undoped and doped CPs. Our method directly measures the temperature gradient and uses Fourier's Law of heat conduction for data interpretation. This technique is advantageous over previous methods because it is simple to use, reliable and fast. The technique does not require any surface treatment and being influenced by supporting substrates. Additionally, this technique requires little sample specimen (e.g. milligram). Using this method, we first discussed the working principle of this technique. Then we reported the thermal conductivity for P3HT and PDPPT polymers at different doping levels with F4TCNQ dopants, discussed the effects of dopants on thermal conductivity with respect to electrical conductivity, crystallinity and molecular packing (e.g. π-π stacking). Our finding indicated out-of-plane thermal conductivity was enhanced due to a higher degree of crystallinity and stronger π-π interactions at a low dopant level (~ 5 wt%). The discovery of measuring fast and accurate out-of-plane thermal conductivity method through Flash-DSC be used to probe thermal conductivity of various doped conjugated polymers to guide the rational design of high performing CPs for thermoelectric device applications.

2. Methodology

2.1 Materials

Poly (3-hexylthiophene-2,5-diyl) (P3HT) was purchased from Rieke Materials with regioregularity higher than 90%. Poly{2,2'-[(2,5-bis(2-hexyldecyl)-3,6-dioxo-2,3,5,6-tetrahydropyrrolo[3,4-c]pyrrole-1,4-diyl)dithiophene]- 5,5'-diyl-alt-thiophen-2,5-diyl}(PDPPT), and poly{[N,N'-bis(2-hexylldecyl)naphthalene-1,4,5,8-bis(dicarboximide)-2,6-diyl]-alt-2,5-thiophene}(NDI(2HD)T) were purchased from Ossila. The p-type dopant, 2,3,5,6-tetrafluoro-7,7,8,8-tetracyanoquinodimethane (F4TCNQ) was purchased from Ossila with a purity higher than 99 %. The doping process was performed by dissolving both CPs and dopants in chlorobenzene (CB) at a temperature of 80 °C with a magnetic stirrer for 8 hours to form a homogenous solution. The stored solution was reheated at 80 °C before preparing films to avoid any aggregation caused by dopants. The weight percentage of dopant was varied from 0 to 20 % for P3HT doped solutions and 0 to 40 % for PDPPT doped solutions.

2.2 Sample Preparation

The testing specimen was obtained by drop casting the solution into a rectangular rubber mold to trap the solution to prepare a bulk film, with a thickness greater than 20 μm to minimize the influence of interfacial thermal resistance.[58] In addition, the solution was evenly spread by pipette to form a homogenous smooth film to reduce the influence of an uneven surface which may result in various heat transport paths. After multiple drop casting processes (> 20 times), the film was peeled off using tweezers from the mold and a small 1x1 mm wrinkle-free piece of the most even part in the center of the film was cut. Afterward, this film was trimmed using a scalpel to cover the heating area on the sample side with a size of 0.6 x 0.6 mm, as shown in **Figure 1a**. The indium size was controlled

to be less than 400 ng to minimize the thermal lag caused by sample size.[59] The bulk film was attached using an animal hair stylus and then moved to the center of the heating area of a circular shape on the sample side. After melt-on (a heating ramp from room temperature to 200 °C) procedure, the testing specimen was stuck on top of the heating area to prevent any possible displacement during the measuring process, as shown in **Figure 1a**. The thermal conductivity experimental set up illustrated in **Figure 1a** displayed the top view from Flash DSC chip. Both sample and reference sides are combined in one chip, unlike conventional DSC which has separate chambers. The CP bulk film was placed at the center of the heating area which is a circular shape on the sample side and indium particles were then placed both on top of CP film for the sample side and directly on top of the heating area for the reference side. A very thin layer of silicon oil was preloaded between the film and sample side substrate[60], as well as In and reference side substrate. Because the film acted as a thermal insulating barrier that influences the heat transfer rate, the film thickness is a crucial quantity to be characterized. A profilometer was used to measure the film thickness. The film thickness indicated here were based on an average value from 3~ 5 different locations. The film roughness was taken into consideration for error propagations. The heating rates for undoped films were from 10 to 110 K/s with an increment of 10 K/s, and the heating rates for doped films were from 10 to 65 K/s and each increment was 5 K/s to avoid the baseline ringing (multiple zig-zag lines covered all testing temperature range) occurred at the relative higher thermal conductible films. Each thermal conductivity measurement for heating scans from 10 to 110 K/s or 10 to 65 K/s was counted as one cycle. The dopant content used in P3HT system was from 0 wt% to 20 wt% since a further increase in dopant content resulted in strong dopant aggregation that caused rough, inhomogeneous, and cracking surfaces. This effect is less problematic for the PDPPT polymer, and higher dopant ratios up to 40 wt% were measured. Thus, the very high dopant ratio (30 wt% and 40 wt%) thermal conductivity experiments were only conducted for PDPPT films.

2.3 Characterization Techniques

A Mettler-Toledo Flash differential scanning calorimeter (Flash DSC 2+) was used for thermal measurements for melting behaviors of indium particles between the sample side and reference side of Flash DSC chip. A Mettler-Toledo DSC (DSC 3+) was used for specific heat capacity measurements for P3HT and PDPPT, where an indium standard was used to calibrate the heat flow and onset of melting temperature at 10 K/min heating rate. All measurements were done under nitrogen gas with a flow rate of 60 ml/min at ambient gas pressure. The film thickness of the testing specimen was recorded by Bruker DektakXT stylus profilometer with a stylus tip radius of 12.5 µm using standard hills and valleys scan for the maximum range of 524 µm over a 2 mm-long area. A Zeiss AX10 microscope was used to monitor the specimen surface image after film was loaded on Flash DSC chip and the surface changes before and after experiments were also captured.

The electrical conductivity and Seebeck coefficient were measured manually using a voltage-sourced two-point probe method and peltier devices, respectively, with pre-patterned bottom contact Au electrodes for 2.5 wt% and 5 wt% doped samples owing to low electrical conductivity. For rest of the doping concentrations, measurements were performed on Netzsch SBA 548 Nemesis thermoelectric set up under an He environment.

Wide angle X-ray scattering (WAXS) of polymeric thin films were performed on samples dropped casted onto aluminum substrates and characterized in transmission scattering mode. Scattering images were recorded on a Pilatus 1M detector (Dectris Inc.) with an exposure time of 15min for those bulk samples. All the scattering data were processed using the Nika software package, in combination with Wavemetrics Igor and WAXStools. Grazing incidence wide angle X-ray scattering (GIWAXS) of polymeric thin films on silicon substrate was performed on a laboratory beamline system (Xenocs Inc. Xeuss 2.0) with an X-ray wavelength of 1.54 Å and sample to detector distance of 15 cm. An incidence angle of 0.2° was used. Samples were kept under vacuum to minimize air scattering. Diffraction images were recorded on a Pilatus 1M detector (Dectris Inc.) with an exposure time of 1.5 h.

Doped P3HT and DPP-based films were measured using a nanoIR3 AFM-IR from Anasys Instruments (Santa Barbara, CA) coupled to a MIRcat-QT™ quantum cascade, mid-infrared laser (frequency range of 917-1700 cm^{-1} and 1900-2230 cm^{-1} and repetition rate of 1,470 kHz). AFM-IR data were collected in tapping mode using a gold-coated AFM probe (spring constant (k): 40 N/m and resonant frequency (fo): 300 kHz). The pulsed, mid-IR laser was tuned to resonance bands unique to each component as determined by FTIR characterization (1452 cm^{-1} for P3HT and 1666 cm^{-1} for DPP). Acquired images were flattened using Analysis Studio software.

3. Results

We first discuss the methodology used to measure the thermal conductivity for conjugated polymeric films. We used Flash DSC to monitor the changes in heat flow initiated from the bottom of the test film to the top surface, where different heat flow rate was associated with heat conduction due to different polymer barriers. **Figure 1a** displays the experimental setup, where details of sample preparation can be found in the experimental section. The thermal conductivity of CPs was quantitatively captured based on the Fourier's Law. The schematic drawing in **Figure 1a** shows different thermal conduction pathways between the sample side and reference side on a Flash DSC chip. On the reference side, a tiny indium (In) particle is in direct contact with a resistive heat source; thus, the onset of melting temperature of indium is in the vicinity of its reported melting temperature of 156.6 °C. On the sample side, another indium particle is placed on the top of the polymer film. To melt the indium particle on the sample side, heat must be transported from the bottom of the polymer film to its top to melt the indium at the top layer following the heat conduction mechanism. Consequently, there should be a

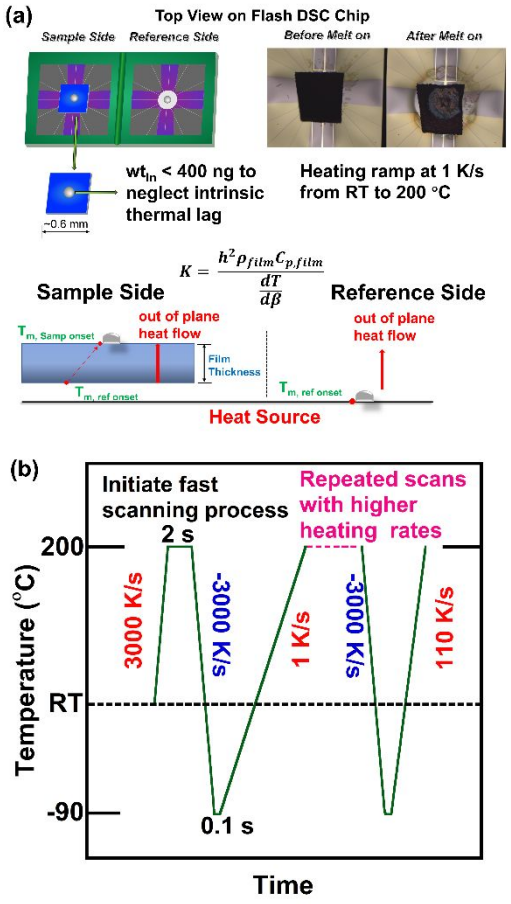

Figure 1. Schematic plots of the experimental setup for measure thermal conductivity for conjugated polymers shown in **a)** Testing specimen location and schematic of heat conduction process for CP film on Flash DSC chip. The thermal conductivity is calculated based on Fourier's Law. **b)** Temperature program for thermal conductivity measurements.

temperature delay between the heating source and the melting of the indium on the sample side.

Next, we discuss how the delay in melting for the indium on the sample can be used to measure the thermal conductivity of the polymer film. The underlying Fourier's Law heat transfer model is explained in the equation shown in **Figure 1a**, K is the thermal conductivity, ρ and h are the density and thickness of film respectively, Cp is the specific heat capacity which is obtained from heat flow $\dot{Q}$ in equation (2), T is the temperature and β is the heating rates. The heat flow is calculated by the following equation:

$$\dot{Q} = -KA\frac{\Delta T}{\Delta h} \quad (2)$$

$$\dot{Q} = mC_{p,film}\beta \quad (3)$$

where A and m are the surface area and mass of the film, expressed as $m = A\Delta h\rho_{film}$. Based on literature results, the reported density of P3HT[61] and PDPPT[62] at 156.6 °C was estimated to be 1.03 g/cm^3 and 1.01 g/cm^3, respectively. The specific heat capacity data was obtained from the heat flow of bulk samples near the melting peak of pure indium (154~156 °C) using conventional DSC based on equation 3 (representative heat flow vs. temperature plots can be found in **Figure S1**).

Therefore, the thermal conductivity equation is combined as the following:

$$K = \frac{h^2\rho_{film}C_{p,film}}{\frac{dT}{d\beta}} \quad (4)$$

where the denominator term is the dependence of the temperature difference between the bottom and top layers of the testing film for various heating rates. By recording the temperature difference between the onset melting temperatures of the indium on the CP film and reference indium at varying heating rates, the difference in two melting temperatures, namely thermal lag, can be plotted against the changing heating rates. In this case, the denominator term in equation 4 is the slope of the curve. Because film thickness plays an important role in the measurements of thermal conductivity, equation 4 can be normalized by thickness so that the denominator is adjusted to d(T/h²)/dβ and defined as M for the remainder of this discussion so that equation 4 is also adjusted accordingly as the following:

$$K = \frac{\rho_{film}C_{p,film}}{M} \quad (5)$$

Flash DSC can control heating rates over three orders of magnitude from 1 K/s to 1000 K/s. This method focuses on the out-of-plane thermal conductivity via the difference in melting temperature of indium with respect to a wide range of heating rates.

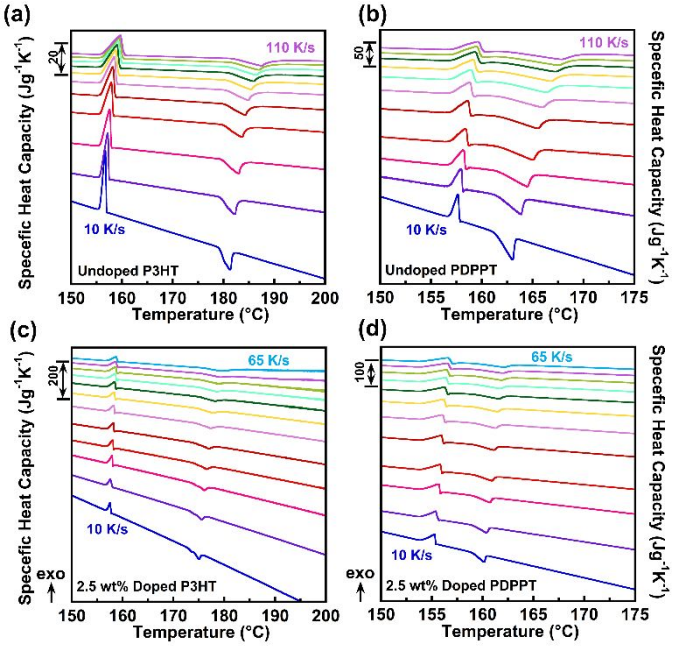

Figure 2. Representative Flash DSC specific heat capacity data plotted with temperature for **a)** undoped P3HT, **b)** undoped PDPPT, **c)** 2.5 wt% doped P3HT, and **d)** 2.5 wt% doped PDPPT, where the heating rates increase from bottom curve to top curve.

The temperature program employed in Flash DSC is displayed in **Figure 1b**, where an initial heating temperature ramp of 3000 K/s was applied to the film to raise the temperature to 200 °C and then held for 2 s to initiate the fast-scanning process. The following cooling step with the same temperature ramp of 3000 K/s was used to quench both the CP film and indium to – 90 °C. The subsequent heating scans with

heating rates ranging from 1 K/s to 110 K/s were selected based on various film thicknesses or dopant ratios to optimize the melting peak signals for indium.

Next, we applied our technique to study the out-of-plane direction thermal conductivity of two representative conjugated polymers: undoped and doped P3HT and PDPPT, respectively. **Figure 2a & 2c** are the representative plots for Flash DSC heat flow versus heating rates for undoped and 2.5 wt% doped P3HT films, respectively. Likewise, **Figure 2b & 2d** display the selective plots for Flash DSC thermal response as a function of heating rates for undoped and 2.5 wt% doped PDPPT films, respectively (other data for doped films at different doping ratios can be found in **Figure S2**). It was clearly observed in both figures that the first melting peak assigned to the indium reference was independent of the heating rate. The second melting peak assigned to indium on the top of the CP film shifted to a higher temperature as heating rates increase. This indicated that thermal lag became appreciable at higher heating rates.

To directly compare the changes in thermal conductivity with respect to various doping levels, the normalized thermal lags against heating rates were plotted in **Figure 3a** and **3b** for undoped/doped P3HT and PDPPT, respectively. The thermal lag is linearly proportional to the increasing heating rates, as expected. As shown in equation 5, the higher slope M indicates lower thermal conductivity. Highly doped films showed larger normalized thermal lag indicates poor thermal conductivity. For other films, the normalized thermal lag with respect to heating rates was calculated and tabulated in **Table 1** (representative statistical analysis shown in **Table S2**). This observation clearly indicates the highest thermal conductivity was achieved for P3HT doped at a 2.5 wt% concentration in **Figure 3a** and PDPPT doped at a 5 wt% concentration in **Figure 3b**.

Based on *M* values retrieved from **Figure 3a & 3b**, the thermal conductivity for undoped and doped films was calculated and presented in **Figure 3c & 3d** for P3HT and PDPPT, respectively. The error bars for thermal conductivity originate from the standard deviations from film thickness measurements and thermal lag vs. heating rates slope fitting results. From the dashed lines shown in **Figure 3 a&b**, one would expect that the thermal lags still exist even when the heating rates are reduced to zero. Based on heat conduction mechanism, heat will spontaneously transport from high temperature area to low temperature area if there is a temperature gradient. To testify this assumption, we applied the slowest heating rates (0.1 K/s) for 2.5 wt% doped P3HT and PDPPT films. The thermal lags for the slowest heating rates films were quantitatively captured by the fitting equations (as shown in **Figure S3**), which is consistent with our assumptions. Thermal conductivity for P3HT increased from 0 to 2.5 wt% doped films and then followed a descending trend. We hypothesized the reduced thermal conductivity was caused by large aggregates of dopant inhibiting the crystalline domains. We later tested this hypothesis using wide angle X-ray scattering (WAXS) and atomic-force microscopy paired with infrared spectroscopy (AFM-IR) and the results will be discussed later. A similar pattern was observed for PDPPT films. However, the maximum thermal conductivity for doped films was achieved at 5 wt%, and 20 wt% and still exhibited a higher thermal conductivity relative to undoped films. This observation was attributed to alleviated dopant aggregation for PDPPT films. Additionally, 40 wt% doped PDPPT film possessed a lower thermal conductivity than undoped samples, which was attributed to reduced crystallinity in highly-doped PDPPT films. All sample physical parameters and thermal conductivity measurements can be found in **Table 1**. We also compared our value to a 3ω method by Linseis Thin Film Analyzer (TFA), where 10 wt% doped PDPPT sample results agreed with our Flash DSC results, as shown in **Table S3**.

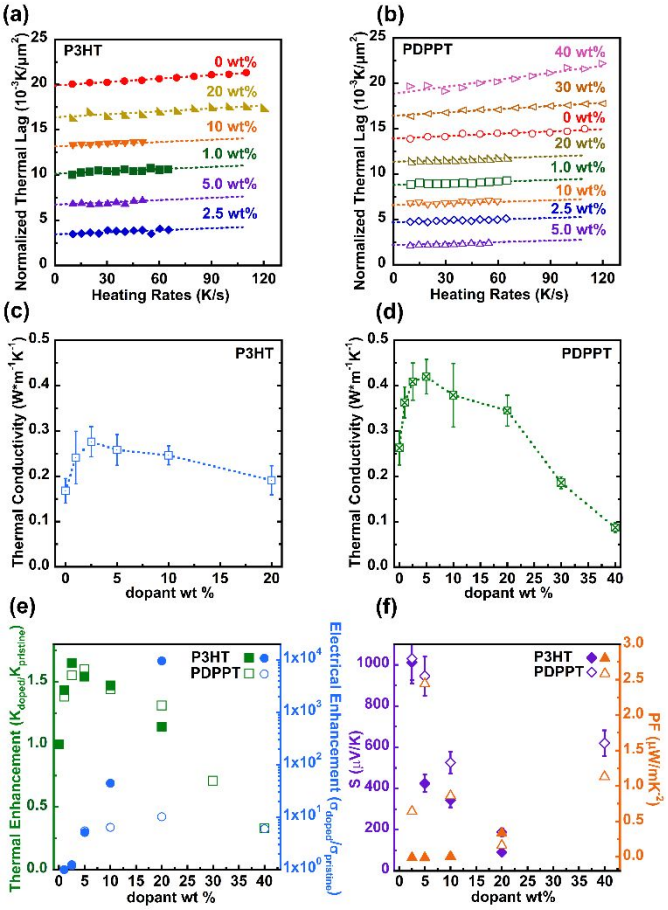

Figure 3. The normalized thermal lags for undoped and doped CPs for **a)** P3HT film and **b)** PDPPT film. The symbols are vertically shifted that the slope M decreases from top to bottom. Thermal conductivity against dopants ratio for **c)** P3HT and **d)** PDPPT **e)** The extent of enhanced thermal conductivity and electrical conductivity plotted against dopant ratio, where green square represents thermal conductivity enhancement and blue circle represents electrical conductivity enhancement. **f)** Seebeck coefficients and the calculated power factor for doped CPs, where purple diamond represents S values and orange triangle represents power factor values. All solid symbols represent P3HT, while open symbols represent PDPPT.

It is well known that the introduction of dopants increases charge carrier mobility in the conjugated polymer system,[63–65] therefore, the increased number of highly active electrons potentially could facilitate heat transport. To correlate the thermal and electrical conductivity of undoped and doped films, **Figure 3e** depicts both the enhancement in thermal conductivity ($K_{doped}/K_{undoped}$) (green square symbols) and electrical conductivity (blue circle symbols) as a function of

dopant. The electrical conductivity was measured by two-probe techniques, where raw data for manual setup can be found in **Figure S4**. In addition, **Figure 3f** displays the Seebeck coefficients (purple diamond symbols) (available raw data shown in **Figure S5**) and the correlated power factors (PF) (orange triangle symbols) against dopant weight percent for the purpose of thermoelectric performance calculations. The thermal conductivity for undoped P3HT and PDPPT is 0.168 and 0.263 W/mK, respectively, which is attributed to higher backbone chain rigidity and shorter π-π stacking distance for PDPPT.[66–68] After doping, both CPs exhibited similar behaviors, where near identical enhancement factors were observed at a dopant ratio ranging from 1 wt% to 10 wt%. For higher dopant ratios (> 20 wt%), PDPPT not only has greater absolute thermal conductivity in comparison to P3HT (0.345 vs. 0.191 W/mK), but also higher enhancement factor (1.31 vs. 1.14). At higher doping levels, P3HT films underwent severe phase separation leading to a rough surface. Beyond 20 wt% dopant level, both electrical conductivity and thermal conductivity for PDPPT began to decline, where reduced electrical conductivity was also reported in the literature due to hindered charge transport pathways[69–71].

Similar trends were observed for Seebeck coefficients measurements between P3HT and PDPPT, where Seebeck coefficients decreased as electrical conductivity increased with higher dopant ratio due to the electrical conductivity and Seebeck conundrum[72]. The electrical conductivity for P3HT monotonically increased with dopant concentrations. In contrast, the electrical conductivity for PDPPT increased up to 20 wt% doping and then decreased which is attributed to a reduction in electron mobility at high doping concentrations[73,74]. The highest power factor for the two polymers was achieved at 20 wt% for P3HT and 5 wt% for PDPPT. This higher performance is attributed to balanced electrical conductivities and Seebeck values. The electrical conductivity, Seebeck coefficient and power factors can be found in **Table 2**.

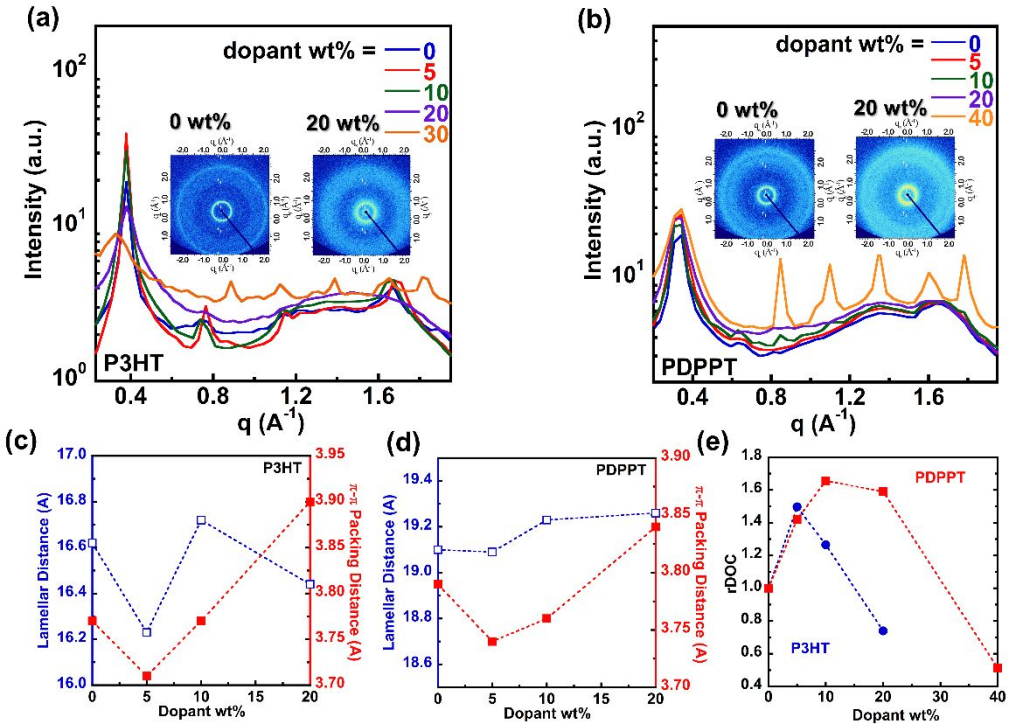

Figure 4. WAXS 1D scattering profile for undoped and doped CP thin films **a)** P3HT and **b)** PDPPT dropcast films respectively, where inset figures are the 2D detector images for 0 and 20 wt% doped films. Lamellar stacking distance and π-π stacking distance as a function of various dopant ratios for **c)** P3HT and **d)** PDPPT **e)** The relative degree of crystallinity for P3HT and PDPPT polymers at different doping ratios, which are calculated based on GIWAXS results.

From a macroscopic perspective, we have observed the dependence of thermal conductivity on doping levels, however, it is worth mentioning that a microscopic understanding is still needed to explain these observations. Here, we provided various molecular-level characterizations using scattering and microscopy techniques to understand morphology change upon doping. We aim to provide the relationship between crystallization/molecular packings and the corresponding influences in measured thermal conductivities. WAXS was performed on doped P3HT and PDPPT films to probe their crystalline structure (**Figure 4**). The 1-D scattering profiles (as shown in **Figure 4a & 4b**) were fitted to report lamellar packing distances from the (100) peak and π-π packing distances from the (010) peak in **Table 3 & 4**. The representative 2D images for 0 and 20 wt% doped dropcast films were shown in the inset figures, where the other dopant levels can be found in **Figure S6**. Lamellar packing distance and π-π packing distance for P3HT and PDPPT are summarized in **Figure 4c & 4d**, respectively. For P3HT thin films, the dopants reduced the π-π packing distance from 3.77 Å for undoped films to a minimum of 3.71 Å for 5 wt% doped films. The similar phenomenon was reported in the

recent work by Fenwick[75] that F4TCNQ doped P3HT showed significantly high thermal conductivity with reduced π-π packing distance from 3.8 to 3.6 Å. Likewise, for PDPPT thin films, the added dopants reduced π-π packing distance from 3.79 Å for undoped films to 3.74 Å at 5 wt% doping levels. This observation indicates that CP films with 5 wt% dopants possessed the strongest π-π interactions compared to other doped films, where π-π packing distance further increased as more dopants were introduced to film. The increased π-π packing distance observed for heavily doped films was associated with the impaired π-π interchain interactions due to larger dopant aggregations, whereas the π-π packing peak disappeared for the largest aggregated 30 wt% P3HT film and 40 wt% PDPPT films. In addition to π-π interactions, the relative degree of crystallinity (rDOC) for all doped CPs were calculated and plotted in **Figure 4e** using grazing incidence wide angle X-ray scattering (GIWAXS). The crystallinity first increased as the doping level increased up to 5 wt% dopant concentration for P3HT and 10 wt% dopant concentration for PDPPT. Beyond this concentration, dopant aggregation increased the number of unreacted dopants and disrupted the crystallites, resulting in lower rDOC for CPs. For semicrystalline CPs, it is expected that crystalline domains increase the mean free path for heat transport due to inhibited disorder scattering, leading to a higher thermal conductivity[76]. The enhancement in rDOC as shown in **Figure 4e** follows the trend of thermal conductivity plots against dopants ratios, which increase from undoped to moderately doped films (e.g. 5~10 % doped films), then decrease to the lowest value. The higher observed rDOC was associated with improved molecular ordering and similar observations were reported in F4TCNQ doped regioregular[77]/regiorandom[78] P3HT systems, where the 2D GIWAXS images can be found in **Figure S7 & S8**.

The thermal conductivity of doped film is closely related to the phase separation between dopants and CPs as well. To better understand the influence of dopant loading on the morphology of P3HT and DPP, doped films were also measured using AFM-IR[79,80]. We first performed FTIR spectroscopy for bulk CPs and F4TCNQ dopants to identify a non-overlap absorbance peak to selectively excite the material of interest, as shown in **Figure S9**. The wavenumber of 1452 cm^{-1} was used to excite the scissoring C-H bond located on the sidechain of P3HT and 1596 cm^{-1} was used to target the F4TCNQ dopant resonance band. As seen in **Figure 5 a&b**, at 5 % doping level, limited aggregation was observed and P3HT formed a fibrous network with domains approximately 40-50 nm in fiber width and the dopant is uniformly dispersed. As dopant loading increased to 20 %, the aggregation size of the dopant increased to between 100-600 nm in diameter (**Figures 5 c&d**). Interestingly, we did not observe any scattering peaks from GIWAXS or WAXS for F4TCNQ at 20 wt% doping level and the dopants formed homogeneous mixed into the amorphous regions of P3HT, as reported in the literature[81,82]. As dopant level increased to 30 wt% in P3HT, the WAXS results (as shown in **Figure 4a**) showed multiple diffraction peaks originated from F4TCNQ indicating that excessive dopants can form crystalline structure, where similar phenomena were observed for 40 wt% doped PDPPT films (as shown in **Figure 4b**).

Doped PDPPT films were also measured using AFM-IR. The wavenumber of 1666 cm^{-1} was used to selectively excite the C=C bond stretching resonance originating from the core of the DPP moiety. As seen in **Figure 5e&f**, for 5 wt% doped PDPPT film, no aggregation was observed for the F4TCNQ dopant and the polymer formed uniform nanodomains at approximately 50-60 nm in diameter. Increasing the dopant concentration to 20 % resulted in clusters of PDPPT domains approximately 100-150 nm in diameter. Meanwhile, the dopants are still uniformly distributed with no sign of large aggregation as shown in the

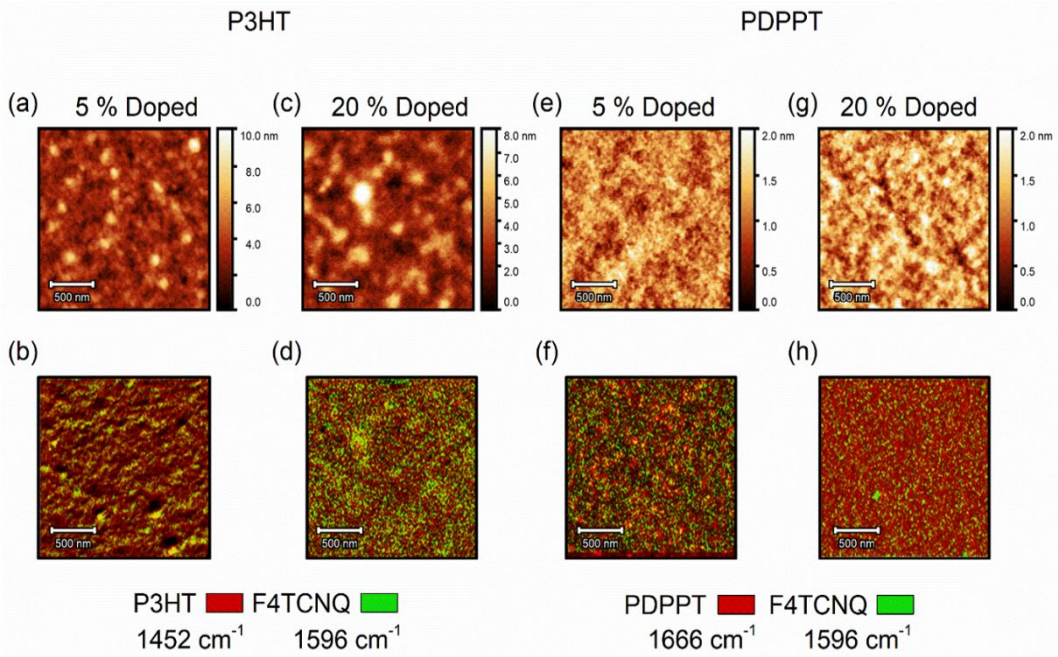

Figure 5. a,c) AFM-IR height images measuring P3HT films doped at 5 % and 20 %. **b,d)** Infrared overlay images corresponding to a/c targeting a resonance wavenumber of P3HT. **e,g)** AFM-IR height images measuring PDPPT films doped at 5 % and 20 %. **f,h)** Infrared images corresponding to e/g targeting a resonance wavenumber of PDPPT. Areas highlighted in red indicate areas containing higher concentrations of the corresponding polymer and areas highlighted in green correspond to higher concentrations of F4TCNQ dopant.

case of P3HT at 20% doping level. In comparison to the doped P3HT films, the F4TCNQ dopant does not induce strong aggregation in the morphology of PDPPT films. The surface morphology for other doping level can be found in **Figure S10**.

Based on the WAXS and AFM-IR measurements, we summarized the mechanism of doping effects on thermal conductivity in **Figure 6**. At a low doping level (e.g. ≤ 5 wt%), F4TCNQ improved the crystallinity of CPs by reducing the π-π packing distance to enhance the π-π interchain interactions, and facilitated heat transport. We observed the highest thermal conductivity in the vicinity of 5 wt% dopant concentration for both CPs. However, as the dopant level continued to increase, excessive dopants induced phase separation between dopants and CPs, and reduced both π-π interactions and degree of crystallinity. This combined effect resulted in a drop in thermal conductivity for heavily doped films (e.g. > 20 wt%). Eventually, severe phase separation significantly impaired both thermal and electrical conductivity for PDPPT resulting in the lowest thermal conductivity and electrical properties for excessively doped films (e.g. >30 wt%).

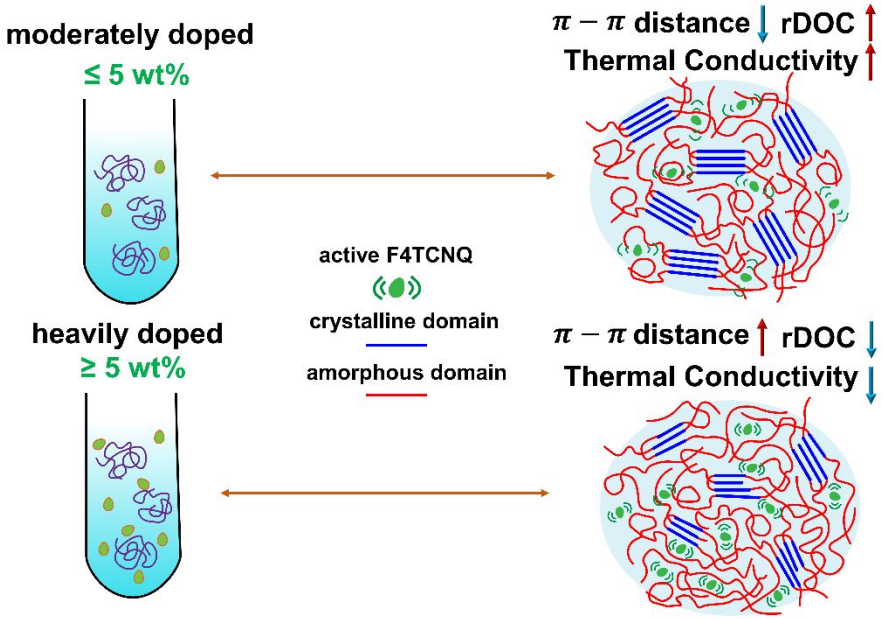

Figure 6. Schematic plots for the effect of dopants on morphology and thermal conductivity for CP films.

4. Discussion

Here, we elaborate on the relationship between thermal conductivity and molecular structural modifications to postulate engineering routes to design high-performance thermoelectric materials. Based on the macroscopic understanding of heat transport for solid materials, thermal conductivity is influenced by both phonon vibrations (also called lattice thermal conductivity K_L) and electron hopping (also called electronic thermal conductivity K_E).[83] The total thermal conductivity can be described by $\boldsymbol{K_T = K_L + K_E}$. For undoped polymers, phonons contributed the majority to thermal conductivity. However, upon doping, the added free electrons began to contribute to thermal conductivity, where the detailed discussions regarding the influence on free electrons on thermal conductivity can be found in SI.

Due to the relatively low enhancements for electrical conductivity, it appears that improved thermal conductivity is primarily due to phonon activity[75]. For inorganic glasses[84], a general equation, $\boldsymbol{K_L = C_v v l_{MFP}}$, can be used to guide the qualitative changes in thermal conductivity. Here, C_v is volumetric heat capacity, v is the average phonon velocity and l_{MFP} is the mean free path for heat transport distance between vibrational scattering events. To correlate structural modifications with the thermal conductivity of CPs, **Figure S11** illustrates thermal conductivities for P3HT, PDPPT, and PNDI(2HD)T (thermal lag plots can be found in **Figure S2**). Similar to outlined experimental approach in this work, we used conventional DSC to obtain the specific heat capacities for all CPs near 156 °C and the results are as follow, $C_{p,PNDI(2HD)T}$ = 2.54 J/gK, $C_{p,PDPPT}$ = 2.20 J/gK, $C_{p,P3HT}$ = 1.98 J/gK. Since $\boldsymbol{C_v = C_p - R}$, the trend of reduced volumetric heat capacity is from PNDI(2HD)T to P3HT. In addition, the melting peak area for those three CPs can be found in **Figure S1**, where the calculated heat of fusion indicated a similar amount of crystals were melted during heating. The elastic modulus of a given polymer was previously reported to influence the average phonon velocity.[85,86] Stiffer polymers possess a higher thermal conductivity than their softer counterparts due to higher phonon velocity. Among three polymers, PNDI(2HD)T has the highest elastic modulus and consequently possesses the highest thermal conductivity, where the elastic moduli for PNDI(2HD)T, PDPPT, and P3HT are 1.0 GPa[66], 0.5 GPa[87] and 0.25 GPa[88], respectively. Combining all these factors, it is reflected in **Figure S11** regarding the guidance of the molecular design on thermal conductivity. As mentioned above, the crystalline domain can increase the mean free path of heat transport distance, leading

to an increase in thermal conductivity. To further demonstrate this is the case, thermal conductivity measurements were also performed for undoped P3HT processed with various solvents to control its crystallinity.[89] For example P3HT processed from a low boiling point solvent in chloroform (CF) has a lower degree of crystallinity than P3HT processed from chlorobenzene (CB). The conventional DSC was used to track the degree of crystallization for the solvent effects on P3HT. As shown in **Figure S12**, the melting peak of P3HT/CF shifted to a lower temperature and the enthalpy of fusion was less than the counterpart of P3HT/CB films. We observed that the thermal conductivity was found to be 0.05 ± 0.01 W/mK for P3HT processed from CF solvent against 0.17 ± 0.03 W/mK for P3HT processed from CB, which confirmed that higher DOC can significantly enhance thermal conductivity, as shown in **Figure S13**. Finally, the stability of our doping films is another concern to address since previous literature reported the dedoping could occur when the dopant was subject to thermal treatment at elevated temperature for more than 10 min.[90] For our work, the experimental process only takes a total of 1 to 10s at higher temperature range (100 to 200 °C) due to rapid heating rates (10 to 110 K/s), consequently, we think the dedpoing will be unlikely to occur in such short time period. Additionally, the instrument intrinsic thermal lags and the reliability & reproducibility for these measurements were investigated, where the detailed discussions can be found in SI. Our reliability test has shown the unchanged melting peaks for the doped films over tens of heating/cooling steps (as shown in **Figure S14**). Therefore, we can confirm that the doping level was maintained during the proposed heating steps.

Conclusion

In summary, we demonstrated a new calorimetric based methodology to directly probe the thermal conductivity for doped CPs for the first time. Using this method, the thermal conductivity of undoped P3HT (0.168 W/mK) and PDPPT (0.263 W/mK) were accurately measured. Additionally, we discovered that the thermal conductivity for doped films initially increased at a low dopant level and then gradually decreased. The morphological study investigated by GIWAXS reveals that the degree of crystallinity peaked for P3HT at 5 wt% and for PDPPT at 10 wt%, then monotonically decreased upon further doping. In addition to changes in rDOC, the π- π packing distance indicated a valley shape where the strongest π- π interactions are found for 10 wt% doped P3HT and 5 wt% doped PDPPT. In combination with both rDOC and π- π interactions, the thermal conductivity for doped CPs exhibited a peak value for polymers with 2.5 wt% to 5 wt% added dopants for P3HT of 0.276 W/mK and PDPPT of 0.420 W/mK, respectively. We further discussed the contribution of electron and phonon in thermal conductivity and concluded that phonon transport dominated in this case. Therefore, CPs with higher crystallinity and rigidity exhibit a higher thermal conductivity. It is expected this new methodology will be valuable for quantitatively measuring thermal conductivity in doped polymers to assist the development of future thermoelectric materials.

Table 1. The summary of thermal conductivity of doped and undoped P3HT and PDPPT

Dopant wt%	P3HT[1]			PDPPT[2]		
	[3]*h* (μm)	[4]*M* (s/m²)	*K* (W/mK)	*h* (μm)	*M* (s/m²)	*K* (W/mK)
0	44.28	$1.23*10^7$	0.168 ± 0.027	32.47	$8.45*10^6$	0.263 ± 0.038
1	21.90	$8.50*10^6$	0.241 ± 0.058	22.08	$6.12*10^6$	0.363 ± 0.034
2.5	49.24	$7.40*10^6$	0.276 ± 0.033	33.37	$5.44*10^6$	0.409 ± 0.041
5	21.94	$8.00*10^6$	0.258 ± 0.034	33.42	$5.30*10^6$	0.420 ± 0.038
10	46.69	$8.76*10^6$	0.246 ± 0.021	24.34	$5.86*10^6$	0.379 ± 0.070
20	42.55	$1.07*10^7$	0.191 ± 0.032	34.69	$6.44*10^6$	0.345 ± 0.034
30				27.36	$1.19*10^7$	0.186 ± 0.013
40				42.84	$2.56*10^7$	0.087 ± 0.011

Note: [1]: P3HT has a M_n of 26,500 g/mol, Đ of 2.6, and regioregularity of 90%;

[2]: PDPPT has a M_n of 31,505 g/mol and Đ of 2.12;

[3]: *h* is film thickness.

[4]: *M* is the normalized slope.

Table 2. The electrical conductivity for undoped and doped P3HT and PDPPT films

Dopant wt%	P3HT			PDPPT		
	σ (S/cm)	S (μV/K)	PF (μW/mK^{-2})	σ (S/cm)	S (μV/K)	PF (μW/mK^{-2})
1	4.5*10^{-5}			5.0*10^{-3}		
2.5	5.4*10^{-5}	1011.5	0.006	6.2*10^{-3}	1030.3	0.66
5	2.3*10^{-4}	424.5	0.004	2.7 *10^{-2}	945.3	2.46
10	2.0*10^{-3}	343.5	0.024	3.2*10^{-2}	525.9	0.88
20	4.3*10^{-1}	90.76	0.354	5.1*10^{-2}	188.1	0.18
40				3.0 *10^{-2}	620.4	1.15

Table 3. Molecular packing for undoped and doped P3HT thin films

Dopant wt%	Lamellar spacing (Å)	Lamellar peak FWHM (Å^{-1})	π -π spacing (Å)	π -π peak FWHM (Å^{-1})
0	16.62	0.049	3.77	0.094
5	16.23	0.033	3.71	0.084
10	16.72	0.048	3.77	0.074
20	16.44	0.096	3.90	0.386

Table 4. Molecular packing for undoped and doped PDPPT thin films

Dopant wt%	Lamellar spacing (Å)	Lamellar peak FWHM (Å^{-1})	π -π spacing (Å)	π -π peak FWHM (Å^{-1})
0	19.10	0.073	3.79	0.299
5	19.09	0.083	3.74	0.321
10	19.23	0.066	3.76	0.262
20	19.26	0.109	3.84	0.296

Conflicts of interest

The authors declare no conflict of interest

Acknowledgements

H.Z., N.P., G.M., and X.G. acknowledge the support by the Office of Naval Research (ONR) under the contract number of N00014-23-1-2063 and H.A., Z, Y. and D.B. thanks the King Abdullah University of Science and Technology (KAUST) Office of Sponsored Research (OSR) under Award No. OSA-CRG2021-4668.

Notes and references

1 G. J. Snyder and E. S. Toberer, *Mater. Sustain. Energy A Collect. Peer-Reviewed Res. Rev. Artic. from Nat. Publ. Gr.*, 2010, 101–110.
2 A. Shakouri, *Annu. Rev. Mater. Res.*, 2011, **41**, 399–431.
3 J.-H. Bahk, H. Fang, K. Yazawa and A. Shakouri, *J. Mater. Chem. C*, 2015, **3**, 10362–10374.
4 A. J. Heeger, *J. Phys. Chem. B*, 2001, **105**, 8475–8491.
5 J. P. Heremans, M. S. Dresselhaus, L. E. Bell and D. T. Morelli, *Nat. Nanotechnol.*, 2013, **8**, 471–473.
6 D. T. Morelli, V. Jovovic and J. P. Heremans, *Phys. Rev. Lett.*, 2008, **101**, 35901.
7 M. D. Nielsen, V. Ozolins and J. P. Heremans, *Energy Environ. Sci.*, 2013, **6**, 570–578.
8 S. Lee, S. Kim, A. Pathak, A. Tripathi, T. Qiao, Y. Lee, H. Lee and H. Y. Woo, *Macromol. Res.*, 2020, **28**, 531–552.
9 B. T. McGrail, A. Sehirlioglu and E. Pentzer, *Angew. Chemie Int. Ed.*, 2015, **54**, 1710–1723.
10 J. Euvrard, A. Revaux, P. A. Bayle, M. Bardet, D. Vuillaume and A. Kahn, *Org. Electron.*, 2018, **53**, 135–140.
11 D. Kiefer, A. Giovannitti, H. Sun, T. Biskup, A. Hofmann, M. Koopmans, C. Cendra, S. Weber, L. J. Anton Koster, E. Olsson, J. Rivnay, S. Fabiano, I. McCulloch and C. Müller, *ACS Energy Lett.*, 2018, **3**, 278–285.
12 X. Yan, M. Xiong, J. T. Li, S. Zhang, Z. Ahmad, Y. Lu, Z. Y. Wang, Z. F. Yao, J. Y. Wang, X. Gu and T. Lei, *J. Am. Chem. Soc.*, 2019, **141**, 20215–20221.
13 K. Shi, F. Zhang, C. A. Di, T. W. Yan, Y. Zou, X. Zhou, D. Zhu, J. Y. Wang and J. Pei, *J. Am. Chem. Soc.*, 2015, **137**, 6979–6982.
14 C. Mai, R. A. Schlitz, G. M. Su, D. Spitzer, X. Wang, S. L. Fronk, D. G. Cahill, M. L. Chabinyc and G. C. Bazan, *J. Am. Chem. Soc.*, 2014, **136**, 13478–13481.
15 T. Park, C. Park, B. Kim, H. Shin and E. Kim, *Energy Environ. Sci.*, 2013, **6**, 788–792.
16 Z. Fan, D. Du, X. Guan and J. Ouyang, *Nano energy*, 2018, **51**, 481–488.
17 N. T. Kemp, A. B. Kaiser, C. Liu, B. Chapman, O. Mercier, A. M. Carr, H. J. Trodahl, R. G. Buckley, A. C. Partridge and J. Y. Lee, *J. Polym. Sci. Part B Polym. Phys.*, 1999, **37**, 953–960.
18 C.-J. Yao, H.-L. Zhang and Q. Zhang, *Polymers (Basel).*, 2019, **11**, 107.
19 J. Liu, X. Wang, D. Li, N. E. Coates, R. A. Segalman and D. G. Cahill, *Macromolecules*, 2015, **48**, 585–591.
20 A. Weathers, Z. U. Khan, R. Brooke, D. Evans, M. T. Pettes, J. W. Andreasen, X. Crispin and L. Shi, *Adv. Mater.*, 2015, **27**, 2101–2106.
21 N. Mermilliod, L. Zuppiroli and B. Francois, *J. Phys.*, 1980, **41**, 1453–1458.
22 H. Li, M. E. DeCoster, C. Ming, M. Wang, Y. Chen, P. E. Hopkins, L. Chen and H. E. Katz, *Macromolecules*, 2019, **52**, 9804–9812.
23 A. B. Chourasia, *Res. J. Mater. Sci.*, 2016, **4**, 1–5.
24 O. Zapata-Arteaga, A. Perevedentsev, S. Marina, J. Martin, J. S. Reparaz and M. Campoy-Quiles, *ACS energy Lett.*, 2020, **5**, 2972–2978.
25 G.-H. Kim, L. Shao, K. Zhang and K. P. Pipe, *Nat. Mater.*, 2013, **12**, 719–723.
26 N. Liu, J. Peters, A. Ramu, J. A. Floro, J. E. Bowers and M. Zebarjadi, *APL Mater.*, 2019, **7**, 21104.
27 D. Kiefer, L. Yu, E. Fransson, A. Gómez, D. Primetzhofer, A. Amassian, M. Campoy-Quiles and C. Müller, *Adv. Sci.*, 2017, **4**, 1600203.
28 R. Shrestha, P. Li, B. Chatterjee, T. Zheng, X. Wu, Z. Liu, T. Luo, S. Choi, K. Hippalgaonkar and M. P. De Boer, *Nat. Commun.*, 2018, **9**, 1–9.
29 V. Singh, T. L. Bougher, A. Weathers, Y. Cai, K. Bi, M. T. Pettes, S. A. McMenamin, W. Lv, D. P. Resler and T. R. Gattuso, *Nat. Nanotechnol.*, 2014, **9**, 384–390.
30 J. Morikawa, J. Tan and T. Hashimoto, *Polymer (Guildf).*, 1995, **36**, 4439–4443.
31 J. Morikawa, C. Leong, T. Hashimoto, T. Ogawa, Y. Urata, S. Wada, M. Higuchi and J. Takahashi, *J. Appl. Phys.*, 2008, **103**, 63522.
32 C. Jensen, M. Chirtoc, N. Horny, J. S. Antoniow, H. Pron and H. Ban, *J. Appl. Phys.*, 2013, **114**, 133509.
33 P. E. Hopkins, J. C. Duda, S. P. Clark, C. P. Hains, T. J. Rotter, L. M. Phinney and G. Balakrishnan, *Appl. Phys. Lett.*, 2011, **98**, 161913.
34 P. E. Hopkins, B. Kaehr, L. M. Phinney, T. P. Koehler, A. M. Grillet, D. Dunphy, F. Garcia and C. J. Brinker, *J. Heat Transfer*.
35 A. J. Schmidt, X. Chen and G. Chen, *Rev. Sci. Instrum.*, 2008, **79**, 114902.
36 D. G. Cahill, *Rev. Sci. Instrum.*, 2004, **75**, 5119–5122.
37 O. Bubnova, Z. U. Khan, A. Malti, S. Braun, M. Fahlman, M. Berggren and X. Crispin, *Nat. Mater.*, 2011, **10**, 429–433.

38 M. Shahi and J. W. Brill, *J. Appl. Phys.*, , DOI:10.1063/1.5050189.
39 M. Rides, J. Morikawa, L. Halldahl, B. Hay, H. Lobo, A. Dawson and C. Allen, *Polym. Test.*, 2009, **28**, 480–489.
40 M. D. Losego, L. Moh, K. A. Arpin, D. G. Cahill and P. V Braun, *Appl. Phys. Lett.*, 2010, **97**, 11908.
41 J. C. Duda, P. E. Hopkins, Y. Shen and M. C. Gupta, *Appl. Phys. Lett.*, 2013, **102**, 251912.
42 Y. Jin, C. Shao, J. Kieffer, K. P. Pipe and M. Shtein, *J. Appl. Phys.*, 2012, **112**, 93503.
43 J. A. Malen, K. Baheti, T. Tong, Y. Zhao, J. A. Hudgings and A. Majumdar, *J. Heat Transfer*.
44 Z. Guo, D. Lee, Y. Liu, F. Sun, A. Sliwinski, H. Gao, P. C. Burns, L. Huang and T. Luo, *Phys. Chem. Chem. Phys.*, 2014, **16**, 7764–7771.
45 X. Wang, V. Ho, R. A. Segalman and D. G. Cahill, *Macromolecules*, 2013, **46**, 4937–4943.
46 P. Jiang, X. Qian and R. Yang, *Rev. Sci. Instrum.*, 2018, **89**, 94902.
47 P. Jiang, B. Huang and Y. K. Koh, *Rev. Sci. Instrum.*, 2016, **87**, 75101.
48 D. Zhao, X. Qian, X. Gu, S. A. Jajja and R. Yang, *J. Electron. Packag. Trans. ASME*, 2016, **138**, 1–19.
49 H. Wang, W. Chu and G. Chen, *Adv. Electron. Mater.*, , DOI:10.1002/aelm.201900167.
50 S.-M. Lee, D. G. Cahill and R. Venkatasubramanian, *Appl. Phys. Lett.*, 1997, **70**, 2957–2959.
51 T. Tong and A. Majumdar, *Rev. Sci. Instrum.*, 2006, **77**, 104902.
52 D. G. Cahill, *Rev. Sci. Instrum.*, 1990, **61**, 802–808.
53 J. P. Feser, E. M. Chan, A. Majumdar, R. A. Segalman and J. J. Urban, *Nano Lett.*, 2013, **13**, 2122–2127.
54 W. Jang, Z. Chen, W. Bao, C. N. Lau and C. Dames, *Nano Lett.*, 2010, **10**, 3909–3913.
55 T. Beechem, L. Yates and S. Graham, *Rev. Sci. Instrum.*, 2015, **86**, 1–12.
56 K. Xie, Y. He, J. Cai and W. Hu, *Thermochim. Acta*, 2020, **683**, 178445.
57 Y. He, X. Li, L. Ge, Q. Qian and W. Hu, *Thermochim. Acta*, 2019, **677**, 21–25.
58 E. T. Swartz and R. O. Pohl, *Rev. Mod. Phys.*, 1989, **61**, 605–668.
59 S. Van Herwaarden, E. Iervolino, F. Van Herwaarden, T. Wijffels, A. Leenaers and V. Mathot, *Thermochim. Acta*, 2011, **522**, 46–52.
60 A. Alesadi, Z. Cao, Z. Li, S. Zhang, H. Zhao, X. Gu and W. Xia, *Cell Reports Phys. Sci.*, 2022, 100911.
61 Regioregular Poly(3-hexylthiophene-2,5-diyl) Supplied by: Merek Batch No.: EE101702 (med. M, https://scholarsphere.psu.edu/resources/f7b9e04f-436e-4b3f-84f6-f5b8f8985221.
62 C. P. Callaway, J. H. Bombile, W. Mask, S. M. Ryno and C. Risko, *J. Polym. Sci.*, 2022, **60**, 559–568.
63 N. Dubey and M. Leclerc, *J. Polym. Sci. Part B Polym. Phys.*, 2011, **49**, 467–475.
64 A. Moliton and R. C. Hiorns, *Polym. Int.*, 2004, **53**, 1397–1412.
65 Y. Xu, H. Sun, A. Liu, H. Zhu, W. Li, Y. Lin and Y. Noh, *Adv. Mater.*, 2018, **30**, 1801830.
66 Z. Cao, S. Zhang and X. Gu, *unpublished data, 2021*, .
67 S. Zhang, M. U. Ocheje, L. Huang, L. Galuska, Z. Cao, S. Luo, Y. Cheng, D. Ehlenberg, R. B. Goodman and D. Zhou, *Adv. Electron. Mater.*, 2019, **5**, 1800899.
68 B. McCulloch, V. Ho, M. Hoarfrost, C. Stanley, C. Do, W. T. Heller and R. A. Segalman, *Macromolecules*, 2013, **46**, 1899–1907.
69 D. Kiefer, A. Giovannitti, H. Sun, T. Biskup, A. Hofmann, M. Koopmans, C. Cendra, S. Weber, L. J. Anton Koster and E. Olsson, *ACS energy Lett.*, 2018, **3**, 278–285.
70 X. Yan, M. Xiong, J.-T. Li, S. Zhang, Z. Ahmad, Y. Lu, Z.-Y. Wang, Z.-F. Yao, J.-Y. Wang and X. Gu, *J. Am. Chem. Soc.*, 2019, **141**, 20215–20221.
71 K. Shi, F. Zhang, C.-A. Di, T.-W. Yan, Y. Zou, X. Zhou, D. Zhu, J.-Y. Wang and J. Pei, *J. Am. Chem. Soc.*, 2015, **137**, 6979–6982.
72 M. A. Haque, S. Kee, D. R. Villalva, W. L. Ong and D. Baran, *Adv. Sci.*, , DOI:10.1002/advs.201903389.
73 M. Koopmans, M. A. T. Leiviskä, J. Liu, J. Dong, L. Qiu, J. C. Hummelen, G. Portale, M. C. Heiber and L. J. A. Koster, *ACS Appl. Mater. Interfaces*, 2020, **12**, 56222–56230.
74 I. H. Jung, C. T. Hong, U. H. Lee, Y. H. Kang, K. S. Jang and S. Y. Cho, *Sci. Rep.*, 2017, **7**, 1–8.
75 T. Degousée, V. Untilova, V. Vijayakumar, X. Xu, Y. Sun, M. Palma, M. Brinkmann, L. Biniek and O. Fenwick, *J. Mater. Chem. A*, 2021, **9**, 16065–16075.
76 S. J. Stuart, A. B. Tutein and J. A. Harrison, *J. Chem. Phys.*, 2000, **112**, 6472–6486.
77 E. Lim, A. M. Glaudell, R. Miller and M. L. Chabinyc, *Adv. Electron. Mater.*, 2019, **5**, 1–11.
78 P. Y. Yee, D. T. Scholes, B. J. Schwartz and S. H. Tolbert, *J. Phys. Chem. Lett.*, 2019, **10**, 4929–4934.
79 H. Zhao, J. J. Shanahan, S. Samson, Z. Li, G. Ma, N. Prine, L. Galuska, Y. Wang, W. Xia and W. You, *Macromol. Rapid Commun.*, 2022, 2200533.
80 M. Xiong, X. Yan, J. Li, S. Zhang, Z. Cao, N. Prine, Y. Lu, J. Wang, X. Gu and T. Lei, *Angew. Chemie*, 2021, **133**, 8270–8278.
81 B. Neelamraju, K. E. Watts, J. E. Pemberton and E. L. Ratcliff, *J. Phys. Chem. Lett.*, 2018, **9**, 6871–6877.
82 D. T. Scholes, S. A. Hawks, P. Y. Yee, H. Wu, J. R. Lindemuth, S. H. Tolbert and B. J. Schwartz, *J. Phys. Chem. Lett.*, 2015, **6**, 4786–4793.
83 M. Goel and M. Thelakkat, *Macromolecules*, 2020, **53**, 3632–3642.
84 C. Kittel, *Phys. Rev.*, 1949, **75**, 972.
85 X. Xie, D. Li, T.-H. Tsai, J. Liu, P. V Braun and D. G. Cahill, *Macromolecules*, 2016, **49**, 972–978.
86 X. Xie, K. Yang, D. Li, T.-H. Tsai, J. Shin, P. V Braun and D. G. Cahill, *Phys. Rev. B*, 2017, **95**, 35406.

87 S. Zhang, A. Alesadi, M. Selivanova, Z. Cao, Z. Qian, S. Luo, L. Galuska, C. Teh, M. U. Ocheje and G. T. Mason, *Adv. Funct. Mater.*, 2020, **30**, 2002221.
88 B. O'Connor, E. P. Chan, C. Chan, B. R. Conrad, L. J. Richter, R. J. Kline, M. Heeney, I. McCulloch, C. L. Soles and D. M. DeLongchamp, *ACS Nano*, 2010, **4**, 7538–7544.
89 R. C. Nieuwendaal, C. R. Snyder and D. M. DeLongchamp, *ACS Macro Lett.*, 2014, **3**, 130–135.
90 H. Hase, K. O'Neill, J. Frisch, A. Opitz, N. Koch and I. Salzmann, *J. Phys. Chem. C*, 2018, **122**, 25893–25899.